metals

MDPI

Article

Erosion Behaviour of API X100 Pipeline Steel at Various Impact Angles and Particle Speeds

Paul C. Okonkwo [1], Rana Abdul Shakoor [1,*], Moustafa M. Zagho [1] and Adel Mohamed Amer Mohamed [2]

[1] Center of Advanced Materials, Qatar University, 2713 Doha, Qatar; paulokonkwo@qu.edu.qa (P.C.O.); mmsalah@qu.edu.qa (M.M.Z.)

[2] Department of Metallurgical and Materials Engineering, Faculty of Petroleum and Mining Engineering, Suez University, 43721 Suez, Egypt; adel.mohamed25@yahoo.com

* Correspondence: shakoor@qu.edu.qa; Tel.: +97-444-036-867

Academic Editor: Hugo F. Lopez

Received: 12 July 2016; Accepted: 31 August 2016; Published: 27 September 2016

Abstract: Erosion is the gradual removal of material due to solid particle impingement and results in a failure of pipeline materials. In this study, a series of erosion tests were carried out to investigate the influence of particle speed and impact angle on the erosion mechanism of API X100 pipeline steel. A dry erosion machine was used as the test equipment, while the particle speed ranged from 20 to 80 m/s and impact angles of 30° and 90° were used as test parameters. The eroded API X100 steel surface was characterized using scanning electron microscope (SEM) and X-ray photoelectron spectroscopy (XPS). The weight loss and erosion rate were also investigated. The results showed that at a 90° impact angle, a ploughing mechanism was occurring on the tested specimens, while material removal through low-angle cutting was the dominant mechanism at lower impact angles. Embedment of alumina particles on the target steel surface, micro-cutting, and low-angle cutting were observed at low impact angles. Therefore, the scratches, cuttings, and severe ploughings observed on some failed oil and gas pipelines could be attributed to the erosion mechanism.

Keywords: API X100 steel; dry erosion; alumina particles; impact angle; particle velocity

1. Introduction

Petroleum products are transported from one region to another through complicated pipeline networks [1,2]. Different grades of carbon steel are used as pipeline materials as they are required to withstand high-pressure environmental conditions [3,4]. However, erosion of the steels has been a major form of failure experienced in the oil and gas industry and is often caused by the impingement of solid particles on the pipeline's surface [5]. Material removal due to solid particle erosion is believed to be a series of impact events that occur in pipelines and cause extensive damage due to a change in the solid-liquid flow direction. The erosion of the steel surface by a stream of solid particles has been an issue of concern for decades due to high material loss and maintenance costs [6,7]. Unfortunately, there is no universal model that can effectively predict all erosion situations [8–10] and development of a reliable and effective model for solid erosion process still remains a challenge. Several attempts have been made to understand the effect of different parameters, such as; temperature, particles size, and microstructure of both the impinging and eroding surfaces on the solid particles erosion process [11–17]. However, each parameter behaves in a manner peculiar to each process and is often complex due to interrelated variables involved [18–24]. Among these parameters, particle velocity and impact angle play critical roles in the erosion process [25–28]. Matsumura et al. [29] conducted erosion tests of pure iron and 304 stainless steel in order to investigate the effect of surface damage at different impact angles due to impinging silica sand particles. The peak erosion rate was found to be

between 30° and 50° for pure iron and 304 stainless steel, respectively. Finnie et al. [6] also reported that peak erosion and wear rate occurred between 15° and 40° for ductile materials. Bukhaiti et al. [25] investigated the effect of impingement angle on slurry erosion behaviour of AISI 1017 steel and high-chromium white cast iron. Their results revealed that different mechanisms occur at different impinging angles for the two different tested materials. Interestingly, several authors [25,29] have shown that peak erosion rate occurs at different impact angles and may be considered for further study. On the other hand, Stachwick et al. [30] showed that for brittle materials, erosion and wear rate increase with increasing impact angle, reaching a peak at 90°. Islam et al. [17] conducted dry erosion tests on API X42 steel using alumina as the impact solid particle. Their result showed that, at a low abrasive feed rate, erosion rate decreased with increasing impact angle. Increased particle velocity resulted in an increase in the erosion rate of API X42 steel.

High-strength low-alloy (HSLA) steels are becoming the material of choice for the projects requiring larger pipelines because of their appreciably low price-to-yield ratio. API X70 and API X80 have been the commonly used pipeline steel grades due to their ability of withstanding the basic erosion-corrosive environment [31,32]. Recently, the petroleum industry has witnessed an outstanding demand for higher strength pipeline steels e.g., API X100 [32] in order to combat the more stringent environment in terms of erosion-corrosion. Mahdi et al. [32] investigated the effect of temperature on erosion-enhanced pitting corrosion behaviour of API X100 steel. Their result showed that the pitting potential decreased, whereas the pitting current densities increased when the electrolyte temperature was increased from 22 °C to 35 °C. Several researchers [33–35] have investigated the corrosion behaviour of the API X100 steel material in different environments. However, the erosion behaviour of this type of steel is limited in the literature.

Based on the studies that were carried out on different steels by several authors, erosion of steels can be classified according to their response to solid particle impingement at different impinging angles [25,26,28,36,37]. Ductile materials belong to the group that plastically deformed with a maximum erosion rate at low impact angles, while brittle materials fracture with a maximum erosion rate at normal impact angles. Despite several studies on the effects of impact angle and speed on the solid particle erosion of these groups of materials [19,23,38–40], efforts are still required to understand the erosion mechanism of API X100 steel by solid particles as this material is widely used in the petroleum industry. Further study on the effect of particle speed on the erosion of API X100 steel at 30° and 90° impact angles becomes necessary. The novelty of this work is to use an erosion tester to effectively investigate and understand the erosion mechanisms of API X100 steel pipeline at different particle speeds and impact angles, which are of practical importance to control the failure of transportation pipeline systems. Understanding the erosion mechanisms of the pipeline steels is critical for the pipelines' safety, as these mechanisms account for different modes of failure. The outcome of the study will provide a better understanding of the underlying mechanism responsible for failure of API X100 steel pipeline used in the petroleum industry.

2. Experimental Procedure

2.1. Material

The alumina and API X100 steel used in this study were supplied by Magnum Engineers, (Peenya Industrial Estate, Bangalore, India) and by Hebei Yineng Pipeline Group Co., Ltd., (Shandong, China), respectively. The API X100 steel specimens used in the tests were cylindrical in shape, of 15.8 mm diameter and 4.7 mm thickness. Prior to each test, the steel specimens were ground using 240, 320, and 600-grit silicon carbide papers. The chemical composition of the API X100 steel used in this study is given in Table 1.

Table 1. Chemical composition of API X100 steel used in the study.

Material	Specimen	Chemical Composition								
API X100 steel	Target Material	C	Mn	Si	Ni	Cr	Mo	Cu	V	Fe
	wt. %	0.164	0.534	0.101	0.017	0.039	0.0012	0.015	0.025	Bal.

2.2. Method

Figure 1 shows the schematic diagram of the erosion test machine, according to the ASTM G76 specification [41], to study the erosion behaviour of API X100 steel impinged with alumina particles at room temperature.

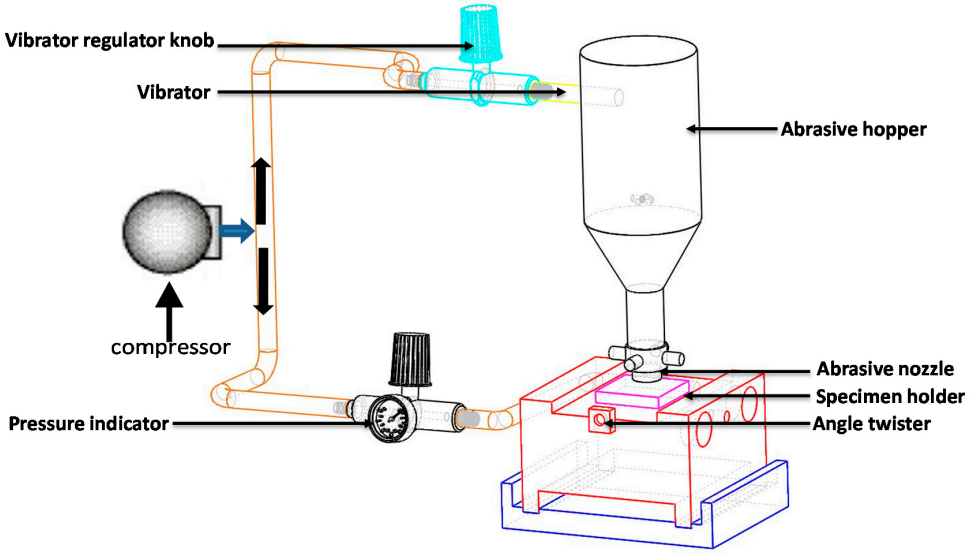

Figure 1. Schematic of the dry erosion machine used to study the erosive behaviour of API X100 steel.

The equipment was designed to allow and control the impingement of the test specimen by the erodent particles through the provision of a sand hopper capable of storing erodent particles and a pneumatic vibrator attached to the sand hopper to enhance free flow of the abrasive particles from the abrasive chamber. The mass flow rate is adjusted by controlling the speed of the sand conveyor and pressure at the vibrator. Alumina particles are fed into the venturi suction from a sand hopper under pressurized air. The impact angle of the particles can be changed by adjusting the angle twister, while the air flow control switch is used to set the desired operating air pressure following the double-disc approach [42].

Particle velocity was determined as a function of pressure using the double disc method detailed elsewhere [42], as shown in Figure 2, while the feed rate of the solid particles was determined by measuring the weight of the abrasive particles coming through the nozzle per unit time. The test parameters used for the erosion of API X100 steel are shown Table 2.

Table 2. Test parameters used for the erosion of API X100 steel.

Test Temperature	Room Temperature
Test gas	Dry compressed air
Particle speed (m/s)	20, 40, 60, 80
Nozzle diameter (mm)	1.5
Test duration (s)	10, 300, 600
Angle of incidence (°)	30, 90
Standoff distance of test specimen (mm)	10

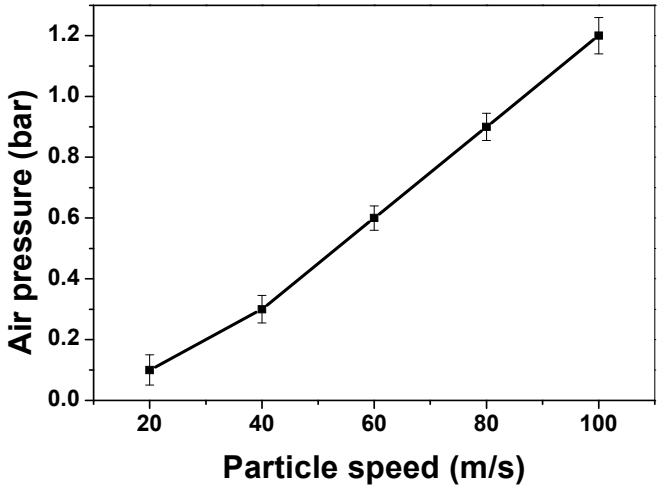

Figure 2. Air jet pressure vs. particle speed.

The alumina particles were forced through a nozzle using a compressed air stream that caused the erodent to impinge the API X100 steel surface at different speeds. The API X100 steel specimens were tested at two impact angles of 30° and 90° and at various particle speeds, speeds as detailed in Table 2. The stand-off distance between the steel specimen and nozzle was kept constant at 10 mm to enhance uniform distribution of the aluminium oxide solid particle stream [43]. The API X100 steel specimen is mounted on the specimen holder facing the nozzle as displayed in Figure 1. The dry erosion tests were run at 10, 300, and 600 s for each of the tested impact angle and particle speeds. Each test was repeated three times for reproducibility. Specimens were weighed before and after each test using a digital balance with accuracy of 0.00001 g to calculate the difference in weight loss.

2.3. Material Characterization

A JEOL JSM-7800F scanning electron microscope (SEM, Peabody, MA, USA) was used to characterise the morphology of the initial surface of the API X100 steel and alumina samples used in this study. Figure 3a,b show the microstructure of the API X100 steel and the alumina particles, respectively. The microstructure of the API X100 steel specimen is composed of fine bainite and ferrite as shown in Figure 3a. The average hardness of ten readings for API X100 steel was 248 ± 6 VHN. The hardness value has been reported for similar materials [44]. The average size of the erodent particles are approximately 80 μm.

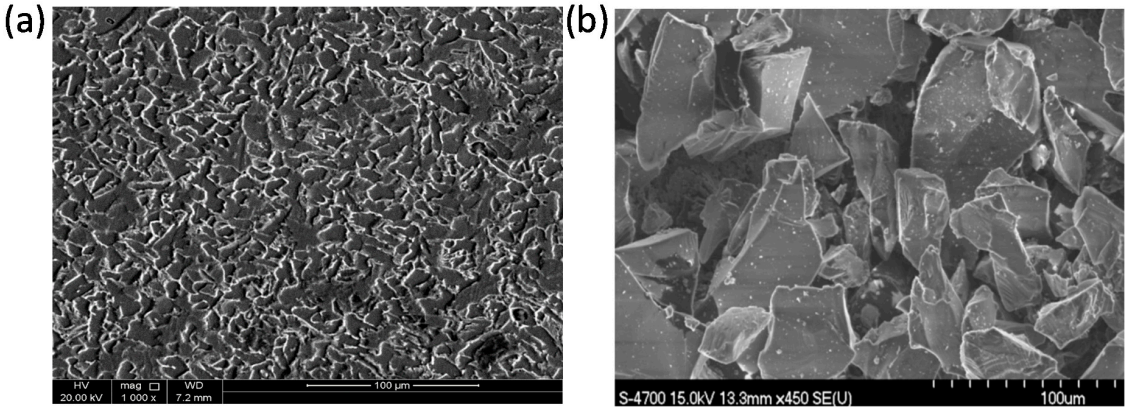

Figure 3. Micrographs of (**a**) API X100 steel and (**b**) alumina particles.

3. Results

The results of API X100 steel specimens subjected to alumina solid particles at four different speeds of 20, 40, 60, and 80 m/s, and impact angles of 30° and 90° are presented in this section. The two angles were selected to investigate the behaviour of the API X100 steel at both low and high impact angles. The SEM and Kratos Axis Ultra DLD X-ray photoelectron spectroscopy (Kratos Analytical Ltd, Manchester, UK) results of the eroded API X100 steel surfaces are also shown and discussed.

3.1. Weight Loss and Erosion Rate Investigation

Figure 4 displays the weight loss of API X100 steel after impinging with alumina particles at different speeds and angles. The results obviously indicate that impinging the API X100 steel surface at 30° and at different particle speeds (Figure 4a) led to higher increasing weight loss compared with impinging the specimens at 90° (Figure 4b). This behaviour can be ascribed to the angle at which the erodent particles strike the target steel surface resulting in higher material removal from the steel surface. Studies have shown that the effect of the impinging angle and particle speed can influence the erosion mechanism and, consequently, result in pipeline failure [45]. It is evident that weight loss of API X100 steel at 30° is much higher than that at the 90° impact angle at the same test duration and particle speed, showing the influence of the impact angle in material loss.

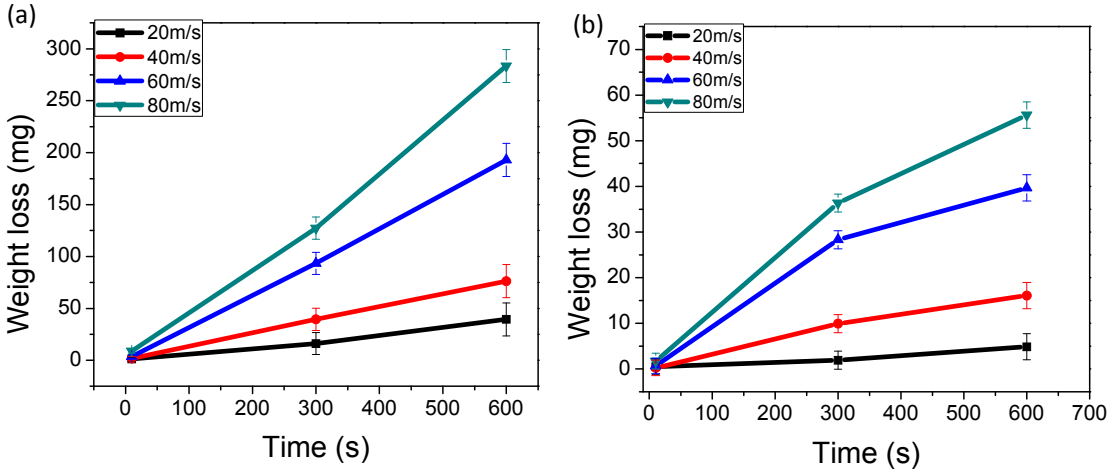

Figure 4. The weight loss of API X100 steel at different speeds for (**a**) 30° and (**b**) 90° impact angles.

Figure 5 shows the erosion rate results for the four particle speeds at 30° and 90° impact angles. The erosion rates were measured from the slope of the weight loss vs. time curves. It is evident that the erosion rates of all API X100 steel specimens increased with increasing particle speed for the two impact angles when they were impinged with alumina solid particles. The erosion rate was calculated by dividing the weight loss of the tested specimen per unit weight of the consumed erodent particles. The results also show that the erosion rate of APIX100 steel impinged at 30° is significantly higher than that of the 90° impact angle (Figure 5).

As can be seen in Figure 5, the erosion rate of the API X100 steel impinged at 30° increased gradually from 20 to 40 m/s. An increase in the impinging speed from 40 to 80 m/s displayed a sharp increase in the erosion rate. The increasing erosion rate as the particle speed is increased in both impact angles can be attributed to more material removal from the target steel surface through different erosion mechanisms, resulting in increasing weight loss. The sharp increase in the erosion rate of the 30° impact angle is also probably associated with the fact that embedded alumina particles can be detached easier from the steel surface of the 30° impact angle than that of 90°.

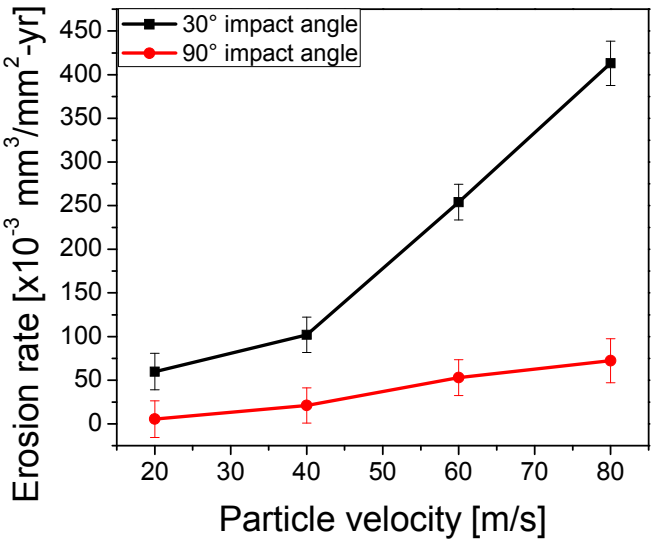

Figure 5. The erosion rate vs. particle speed for 30° and 90° impact angles.

3.2. Erosion Mechanisms of the Eroded Steel Surfaces at Different Angles and Particle Speeds

3.2.1. Erosion Mechanisms of the Eroded API X100 Steel at 20 m/s

Figure 6a displays the results of the tests conducted at 20 m/s and 30° impact angles for 10 s. As can be seen, embedment of alumina particles on the targeted steel surface is evident. As the test duration was increased to 300 s under the same condition, a micro cutting mechanism accompanied with embedment of alumina particles on the steel surface are prevailing at this test condition (Figure 6b). Increasing the test duration to 600 s showed a further increase in the severity of the cutting action observed on the API X100 steel surface (Figure 6c).

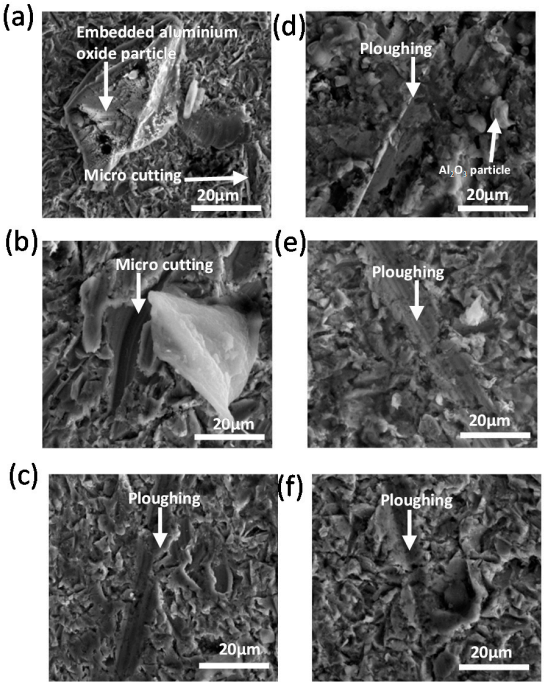

Figure 6. SEM micrographs of 20 m/s at 30° for (**a**) 10 s; (**b**) 300 s; and (**c**) 600 s; and at 90° for (**d**) 10 s; (**e**) 300 s; and (**f**) 600 s.

The SEM micrographs at the 90° impact angle and 20 m/s for 10 s show ploughing of the API X100 steel surface (Figure 6d). Evidence of increasing ploughing width as the test duration increased to 300 s was also observed, as shown in Figure 6e. It could be seen that ploughing observed at a test duration of 600 s has increased in the ploughing width compared to the 10 and 300 s tests with evidence of multiple ploughings (Figure 6f).

3.2.2. Erosion Mechanisms of the Eroded API X100 Steel at 40 m/s

The eroded surface of API X100 steel at 30° impact angle for 40 m/s and 10 s duration is shown in Figure 7a. The feature observed at this test condition is typical of cuttings as reported by Islam et al. [46], where it was shown that cutting occurs when the embedded material that initially embedded into the metal matrix at low particle speed attains enough kinetic energy at speed or test duration to cut the surface in the form of metallic chips (Figure 7a). As the test duration was increased to 300 s under the same particle speed, the cutting features increase in width on the steel surface (Figure 7b). When the test duration was increased further to 600 s, similar features to that seen at 300 s test were evident (Figure 7c). This result suggests that the mechanism did not change when the test duration was increased from 300 to 600 s, but increased the severity of the prevailing mechanism.

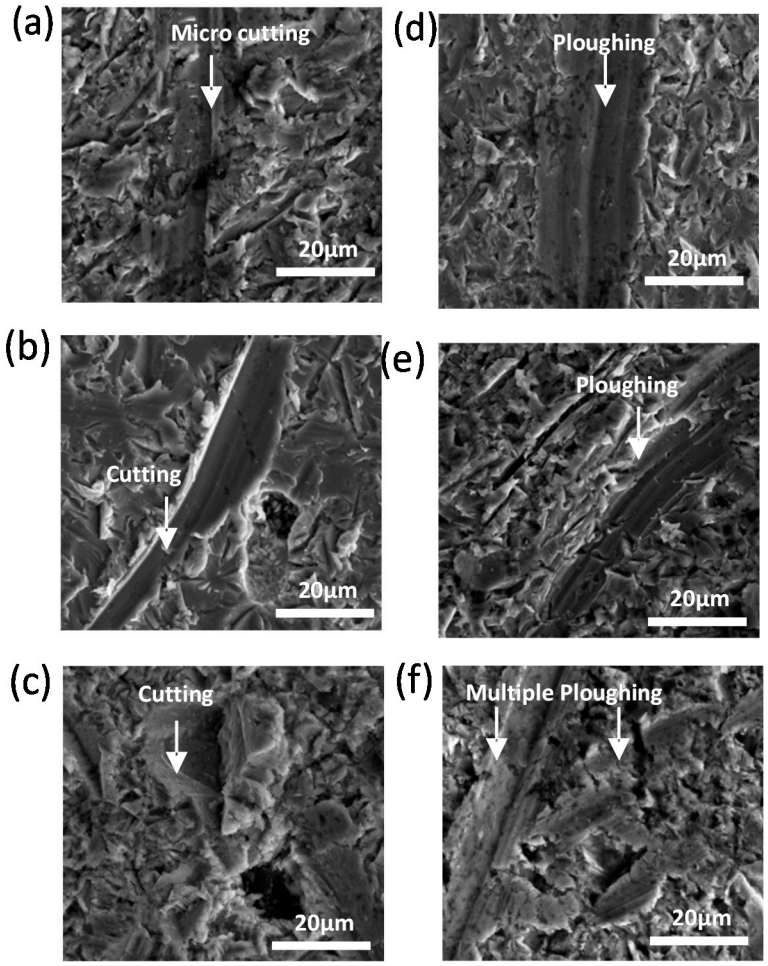

Figure 7. SEM micrographs of 40 m/s at 30° for (**a**) 10 s; (**b**) 300 s; and (**c**) 600 s; and at 90° for (**d**) 10 s; (**e**) 300 s; and (**f**) 600 s.

Figure 7d shows the ploughing mechanism observed when the test was carried out at 40 m/s and 90° impact angle for 10 s. At this test condition, the ploughing of the API X100 steel surface was larger in size compared to that observed at the 20 m/s particle speed (Figure 6d). It is also observed

that the number of ploughings has increased as the test duration was increased from 10 to 300 s. When the test duration was further increased to 600 s, at the same 90° impact angle, multiple ploughings appeared on the eroded steel surface (Figure 7f).

3.2.3. Erosion Mechanisms of the Eroded API X100 Steel at 60 m/s

Figure 8a displays the damage that occurred on the API X100 steel surface at 60 m/s and 30° for 10 s. Multiple cuttings were observed at this test condition (Figure 8a). The SEM micrographs of the eroded specimens performed at 60 m/s and 30° for 300 s are dominated by the transition of mixed-mechanism with cutting and low angle cutting (Figure 8b).

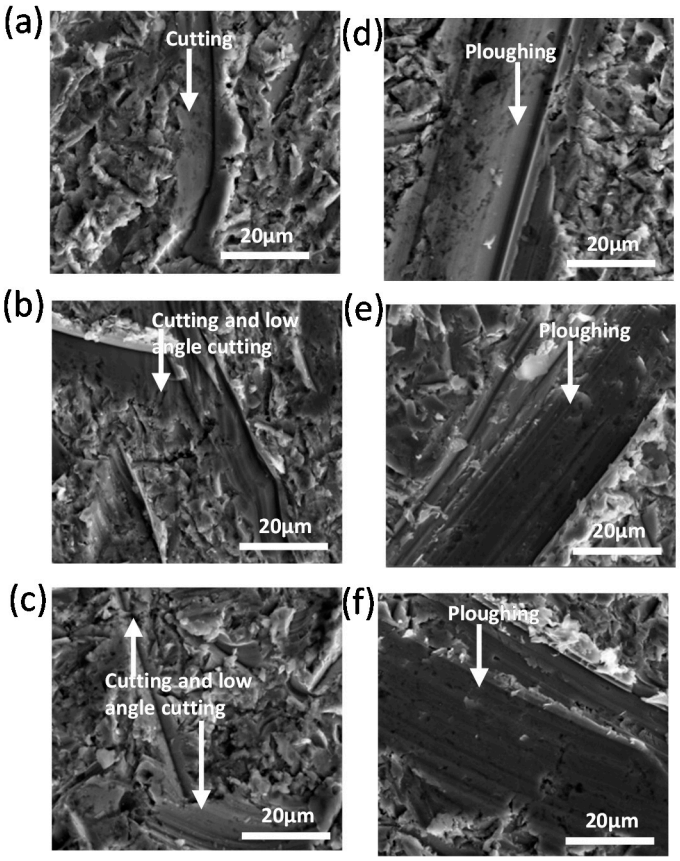

Figure 8. SEM micrographs of 60 m/s at 30° for (**a**) 10 s; (**b**) 300 s; and (**c**) 600 s; and at 90° for (**d**) 10 s; (**e**) 300 s; and (**f**) 600 s.

When the test duration was increased to 600 s under the same condition, cutting of the steel surface through low-angle cutting was observed to be the active erosive mechanism (Figure 8c). For the test performed at 60 m/s, 90°, and different durations, ploughings of different sizes were observed on the eroded API X100 steel surfaces (Figure 8d–f). The ploughing erosion mechanism has also been recently observed for dry erosion API X42 steel at a similar impact angle [45].

3.2.4. Erosion Mechanisms of the Eroded API X100 Steel at 80 m/s

The SEM micrographs of the eroded surface of specimens under 80 m/s speeds at a 30° impact angle and various durations are shown in Figure 9. It can be seen that cutting mechanism was the active mechanism at the 30° impact angle for 10 and 300 s tests (Figure 9a,b). At 600 s/30° impact angle, the eroded specimens were dominated with multiple cuttings (Figure 9c).

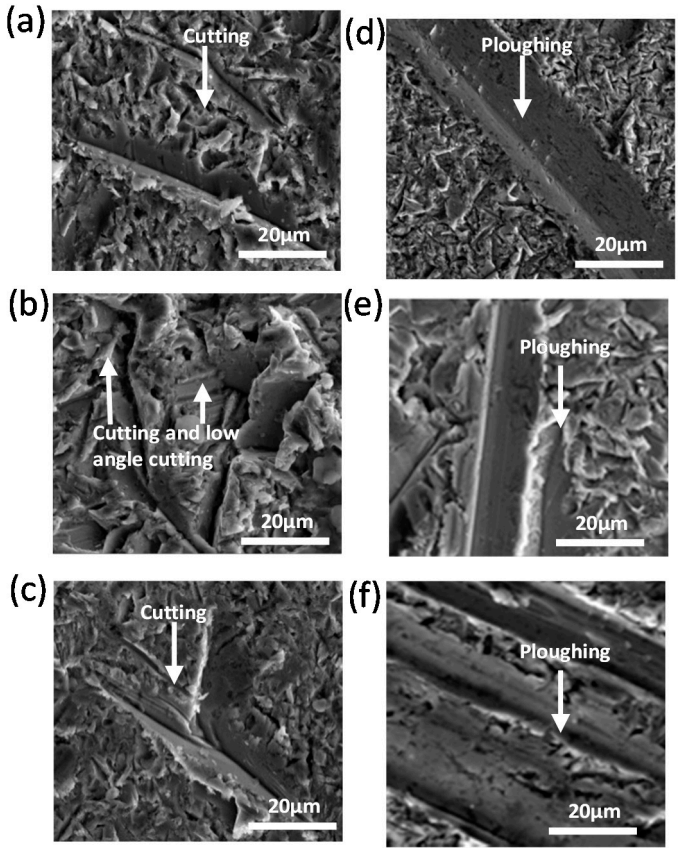

Figure 9. SEM micrographs of 80 m/s at 30° for (**a**) 10 s; (**b**) 300 s; and (**c**) 600 s; and at 90° for (**d**) 10 s; (**e**) 300 s; and (**f**) 600 s.

The SEM micrographs of the eroded API X100 steel surface at 80 m/s and 90° impact angle for different test durations are shown in Figure 9d–f. The ploughing mechanism is evident at this test condition. It is interesting to observe the increase in the ploughing width as the test duration is increased for the same particle speed. This can be attributed to the effect of impingement time on the erosion of the target steel specimens. There is also a distinct trend in the overall mechanism as the test durations were increased. Ploughing of about 20 µm in width was observed on the API X100 steel surface at 300 s. It is significant to note that the number of ploughings increased when the test duration was increased to 600 s (Figure 9f).

Ploughing is believed to occur by sliding of the horizontal component of the impingement solid particles that bombard the target steel surface and reflect in different directions [46]. Furthermore, severity in the ploughing mechanism at a normal impact angle is speculated to be enhanced by the hardness of the steel material.

3.3. XPS Results

Figure 10 shows the XPS survey spectrum of the corroded API X100 steel samples at the 90° impact angle and 80 m/s particle speed. Different peaks in the XPS spectrum are generated because of sputtering of the eroded API X100 steel with Ar^+ ions at different energy levels.

XPS mapping was employed to give further insight into the interaction of the alumina erodent particles and the target API X100 steel compositional elements. The eroded steel surfaces were mapped for elemental distribution. During the erosion process, some of the elements from either surface may be transferred to the other. This will be picked up by the XPS mapping. High-resolution scans performed at 0.1 eV step over the eroded API X100 steel surface, showing a peak at 709.82 eV, which indicates the presence of Fe and is consistent with the previous studies [47]. In addition, the peak observed at

about 713.53 eV is also evident of Fe^{3+} compound. The C 1 s high-resolution XPS spectrum of eroded APIX100 steel at 80 m/s and 90° impact angle indicates two peaks of carbon at different binding energies, which also belongs to the target API X100 steel material.

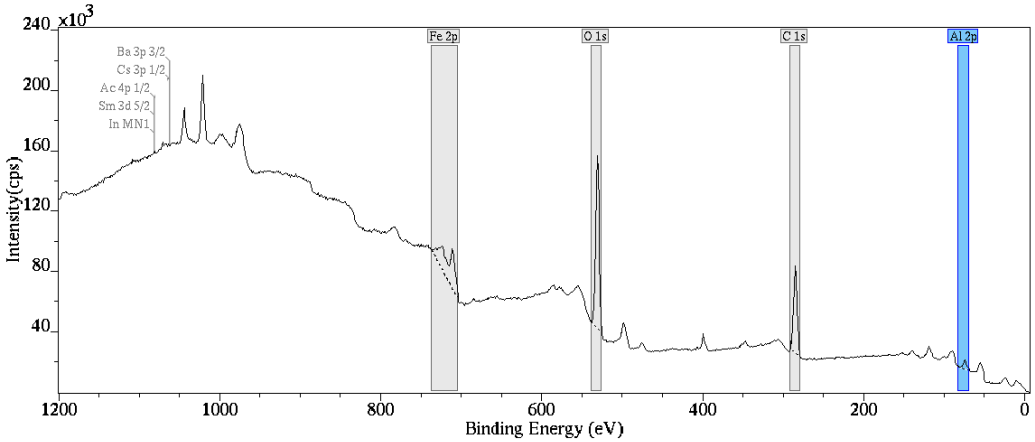

Figure 10. XPS fitting spectra obtained from survey spectrum of eroded API X100 steel at a 90° impact angle and 80 m/s particles speed.

However, the peak at 74.1 eV binding energy can be associated to the presence of aluminium on the API X100 steel surface [48]. It can be concluded that Fe and C found on the eroded API X100 steel surface belong to the target steel specimens, while the aluminium found on the eroded API X100 steel surface is of the erodent solid particles.

Considering the chemical composition of the erodent particles, it can be clearly seen that there is a transfer of the erodent particles to the API X100 steel surface during erosion process. This consolidates the finding of this work showing embedment and transfer of alumina particles to the API X100 steel surface during the erosion process, which may be responsible for the cutting and ploughing mechanisms observed on the eroded steel surface.

4. Discussion

The high erosion rate of API X100 steel at the 30° impact angle compared to the 90° impact angle as the particle speed was increased, (Figure 2), is typical for ductile material behaviour and is in good agreement with reports by many authors [25,26,37]. High abrasive particle flow rates cause a higher interaction between incoming and rebounding particles in the region between the nozzle and target material. The gas pressure induces the force driving the abrasive solid particles onto the target material surface resulting in different erosive mechanisms.

At 20 m/s and 30° impact angle cutting, which later mixed with low angle cutting as the test duration was increased, is seen (Figure 8a–c). Embedment of alumina particles on the target steel surface at 20 m/s for the 30° impact angle could be attributed to low particle velocity and low bombarding kinetic energy. Under this low particle speed condition, the alumina particles may not have enough energy and, hence, embedded into the steel matrix as reported by Md et al. [17]. As the particles speed was increased to 40 m/s at 30° impact angle, the eroded steel surface is cut in "disc–shape" by the bombarding alumina particles. It is also well known that when surfaces impact on another during a repeated contact, the contact induces an alternating subsurface shear stress and plastic strain [49]. Other authors [17,26] have reported that micro cutting and repeated plastic deformation, followed by metal cutting, are associated with material removal mechanisms in ductile materials as observed in this study (Figure 6a–c). Material removal from the target API X100 steel surface through micro cutting and ploughing became more prevalent as the particle speed was increased to 40 m/s at the 30° impact angle.

However, at high particle speed (60 m/s), the solid particles acquire enough energy to cut the target steel surface in the form of metallic chips. It has also been reported [50,51] that metal removal under low impact angle and high speed conditions occurs by the low-angle metal cutting process as observed in this study (Figure 9a–c). On repeated contact, subsurface plastic strain is built up with increasing cycles resulting in formation of pits on the surfaces, as seen when the test was conducted at 80 m/s and 30°. With respect of the tests performed at the 90° impact angle, evidence of ploughings in all of the tests conducted at lower particle speeds indicates that the ploughing mechanism is the operative erosion mechanism (Figure 6d–f and Figure 7d–f). On the other hand, the SEM results of API X100 steel surfaces (Figure 8a–c and Figure 9a–c) conducted at higher particles speeds and the 90° impact angle (Figure 8d–f and Figure 9d–f) provide evidence that multiple ploughings of the API X100 steel surface were the prevailing erosion mechanisms. An increase in particle speed or test duration did not change the mechanism observed at high impact angle tests. It is believed that the increase in the particle speed or test time may result in a decrease in the ploughing mechanism as previously pointed out by other authors [25,42,46], where it was revealed that particle speed has a significant impact on the erosion mechanism of solid particles. It is also believed that, at higher particles speeds, the elastic strain energy is high enough and may exceed the strain energy of the target materials [8,36]. Under this condition, plastic deformation of the target surface results in micro cutting and ploughing of the target steel surface. For the stream particle erosion process, the impinging and reflecting alumina particles may collide and the direction of the impinging particles may change [52,53], as seen in this study when the tests were performed at the 90° impact angle.

When the impact angle is increased under this condition, the sliding component of the particles' speed may plough the target surface as well, depending on the rotation of abrasive particles after impact on the target surface [9,36]. This observation was supported by a recent study of Al-Bukhaiti et al. [25], where the ploughing mechanism of AISI 1017 steel was observed on the target steel surface between impact angles of 15° and 75°, which is in close agreement with the observation of this study. It could then be inferred that the ploughing mechanism seen at the 90° impact angle is influenced by material properties of the target and erodent materials. In the current work, as the particles speed is increased at the 90° impact angle, the dominant erosion mechanism of ploughing intensified with the increase in the width and number of ploughings found on the API X100 steel surface. This highlights the effect of the test time and associated mechanism as the particle speed was increased at high impact angles. These results also suggest that the erosion of API X100 steel used in oil and gas transportation pipelines could be strongly influenced by solid particles speed, impingement time, and impact angle. The result is, therefore, recommended for industrial application in the offshore pipelines, tubing, and pipe fittings industry.

5. Conclusions

The study of the effect of particles velocity and impact angle on the erosion behaviour and mechanisms of API X100 steel has led to the following conclusions:

1. The weight loss and erosion rate of API X100 steel increases with increasing particle speed for the impact angles considered in this study. The increase in weight loss and erosion rate is attributed to increasing material removal from the target API X100 steel surfaces as the speed and test duration was increased.
2. SEM examination clearly showed that ploughing mechanism dominated the 90° impact angle irrespective of the particles speed. It was assumed that the ploughing mechanism observed at the 90° impact angle may be influenced by the material property and test time.
3. Examination of the eroded API X100 steel surface impinged at the 30° impact angle and speed revealed that material removal, dominated by the transition of the mixed-mode with cutting and low-angle metal cutting were the prevailing mechanisms.

4. SEM and XPS analyses confirm the transfer of the erodent alumina particles to the target API X100 steel surfaces during the erosion process.
5. The severity in the ploughing erosion mechanisms of API X100 steel observed in this study may be responsible for the failure of oil and gas steel pipelines, and further study may consider selection of appropriate coatings to increase the resistance of the API X100 steel to erosion.

Acknowledgments: This publication was made possible by NPRP Grant 6-027-2-010 from the Qatar National Research Fund (a member of the Qatar Foundation). Statements made herein are solely the responsibility of the authors.

Author Contributions: Paul C. Okonkwo, R.A. Shakoor and A.M.A. Mohamed conceived and designed the experiments; Paul C. Okonkwo and Moustafa M. Zagho performed the experiments; R.A. Shakoor and A.M.A. Mohamed supervised experimental work and data analysis; R.A. Shakoor and A.M.A. Mohamed contributed the analysis tools and reviewed the manuscript; and Paul C. Okonkwo wrote the manuscript.

Conflicts of Interest: The authors declare no conflict of interest.

References

1. Najibi, H.; Rezaei, R.; Javanmardi, J.; Nasrifar, K.; Moshfeghian, M. Economic evaluation of natural gas transportation from Iran's South-Pars gas field to market. *Appl. Therm. Eng.* **2009**, *29*, 2009–2015. [CrossRef]
2. Thomas, S.; Dawe, R.A. Review of ways to transport natural gas energy from countries which do not need the gas for domestic use. *Energy* **2003**, *28*, 1461–1477. [CrossRef]
3. Das, S.K.; Munda, P.; Chowdhury, S.G.; Das, G.; Singh, R. Effect of microstructures on corrosion and erosion of an alloy steel gear pump. *Eng. Fail. Anal.* **2014**, *40*, 89–96. [CrossRef]
4. Hairil Mohd, M.; Paik, J.K. Investigation of the corrosion progress characteristics of offshore subsea oil well tubes. *Corros. Sci.* **2013**, *67*, 130–141. [CrossRef]
5. Postlethwaite, J.; Dobbin, M.H.; Bergevin, K. The Role of Oxygen Mass Transfer in the Erosion-Corrosion of Slurry Pipelines. *Corrosion* **1986**, *42*, 514–521. [CrossRef]
6. Finnie, I. Erosion of surfaces by solid particles. *Wear* **1960**, *3*, 87–103. [CrossRef]
7. Neilson, J.H.; Gilchrist, A. Erosion by a stream of solid particles. *Wear* **1968**, *11*, 111–122. [CrossRef]
8. Sundararajan, G.; Shewmon, P.G. A new model for the erosion of metals at normal incidence. *Wear* **1983**, *84*, 237–258. [CrossRef]
9. Hutchings, I.M. A model for the erosion of metals by spherical particles at normal incidence. *Wear* **1981**, *70*, 269–281. [CrossRef]
10. O'Flynn, D.J.; Bingley, M.S.; Bradley, M.S.A.; Burnett, A.J. A model to predict the solid particle erosion rate of metals and its assessment using heat-treated steels. *Wear* **2001**, *248*, 162–177. [CrossRef]
11. Andrews, D.R.; Field, J.E. Temperature dependence of the impact response of copper: erosion by melting. *J. Phys. D Appl. Phys.* **1982**, *15*, 2357. [CrossRef]
12. Bousser, E.; Martinu, L.; Klemberg-Sapieha, J.E. Effect of erodent properties on the solid particle erosion mechanisms of brittle materials. *J. Mater. Sci.* **2013**, *48*, 5543–5558. [CrossRef]
13. Maasberg, J.A.; Levy, A.V. Erosion of elevated-temperature corrosion scales on metals. *Wear* **1981**, *73*, 355–370. [CrossRef]
14. Gat, N.; Tabakoff, W. Some effects of temperature on the erosion of metals. *Wear* **1978**, *50*, 85–94. [CrossRef]
15. Sundararajan, G.; Roy, M. Solid particle erosion behaviour of metallic materials at room and elevated temperatures. *Tribol. Int.* **1997**, *30*, 339–359. [CrossRef]
16. López, D.; Congote, J.P.; Cano, J.R.; Toro, A.; Tschiptschin, A.P. Effect of particle velocity and impact angle on the corrosion-erosion of AISI304 and AISI420 stainless steels. *Wear* **2005**, *259*, 118–124. [CrossRef]
17. Islam, M.A.; Farhat, Z.N. Effect of impact angle and velocity on erosion of API X42 pipeline steel under high abrasive feed rate. *Wear* **2014**, *311*, 180–190. [CrossRef]
18. Head, W.J.; Harr, M.E. The development of a model to predict the erosion of materials by natural contaminants. *Wear* **1970**, *15*, 1–46. [CrossRef]
19. Wang, Y.-F.; Yang, Z.-G. Finite element model of erosive wear on ductile and brittle materials. *Wear* **2008**, *265*, 871–878. [CrossRef]

20. Buijs, M.; Houten, K.K. Three-body abrasion of brittle materials as studied by lapping. *Wear* **1993**, *166*, 237–245. [CrossRef]
21. Evans, A.G.; Wilshaw, T.R. Quasi-static solid particle damage in brittle solids-I. Observations analysis and implications. *Acta Metall.* **1976**, *24*, 939–956. [CrossRef]
22. Wood, R.J.K. Erosion-corrosion interactions and their effect on marine and offshore materials. *Wear* **2006**, *261*, 1012–1023. [CrossRef]
23. Dhar, S.; Krajac, T.; Ciampini, D.; Papini, M. Erosion mechanisms due to impact of single angular particles. *Wear* **2005**, *258*, 567–579. [CrossRef]
24. Stack, M.M.; Pungwiwat, N. Particulate erosion-corrosion of Al in aqueous conditions: Some perspectives on pH effects on the erosion-corrosion map. *Tribol. Int.* **2002**, *35*, 651–660. [CrossRef]
25. Al-Bukhaiti, M.A.; Ahmed, S.M.; Badran, F.M.F.; Emara, K.M. Effect of impingement angle on slurry erosion behaviour and mechanisms of 1017 steel and high-chromium white cast iron. *Wear* **2007**, *262*, 1187–1198. [CrossRef]
26. Manisekaran, T.; Kamaraj, M.; Sharrif, S.M.; Joshi, S.V. Slurry erosion studies on surface modified 13Cr-4Ni steels: Effect of angle of impingement and particle size. *J. Mater. Eng. Perform.* **2007**, *16*, 567–572. [CrossRef]
27. Lindsley, B.A.; Marder, A.R. The effect of velocity on the solid particle erosion rate of alloys. *Wear* **1999**, *225–229*, 510–516. [CrossRef]
28. Oka, Y.I.; Ohnogi, H.; Hosokawa, T.; Matsumura, M. The impact angle dependence of erosion damage caused by solid particle impact. *Wear* **1997**, *203–204*, 573–579. [CrossRef]
29. Matsumura, M.; Oka, Y.; Hiura, H.; Yano, M. The Role of Passivating Film in Preventing Slurry Erosion-Corrosion of Austenitic Stainless Steel. *ISIJ Int.* **1991**, *31*, 168–176. [CrossRef]
30. Stachowiak, G.; Batchelor, A.W. *Engineering Tribology*; Butterworth-Heinemann: Boston, MA, USA, 2001.
31. Islam, M.A.; Farhat, Z.N.; Ahmed, E.M.; Alfantazi, A.M. Erosion enhanced corrosion and corrosion enhanced erosion of API X-70 pipeline steel. *Wear* **2013**, *302*, 1592–1601. [CrossRef]
32. Mahdi, E.; Rauf, A.; Eltai, E.O. Effect of temperature and erosion on pitting corrosion of X100 steel in aqueous silica slurries containing bicarbonate and chloride content. *Corros. Sci.* **2014**, *83*, 48–58. [CrossRef]
33. Al-Mansour, M.; Alfantazi, A.M.; El-boujdaini, M. Sulfide stress cracking resistance of API-X100 high strength low alloy steel. *Mater. Des.* **2009**, *30*, 4088–4094. [CrossRef]
34. Mustapha, A.; Charles, E.A.; Hardie, D. Evaluation of environment-assisted cracking susceptibility of a grade X100 pipeline steel. *Corros. Sci.* **2012**, *54*, 5–9. [CrossRef]
35. Gadala, I.M.; Alfantazi, A. Electrochemical behavior of API-X100 pipeline steel in NS4, near-neutral, and mildly alkaline pH simulated soil solutions. *Corros. Sci.* **2014**, *82*, 45–57. [CrossRef]
36. Hutchings, I.M. Deformation of metal surfaces by the oblique impact of square plates. *Int. J. Mech. Sci.* **1977**, *19*, 45–52. [CrossRef]
37. Hutchings, I.M.; Winter, R.E. Particle erosion of ductile metals: A mechanism of material removal. *Wear* **1974**, *27*, 121–128. [CrossRef]
38. Fuyan, L.; Hesheng, S. The effect of impingement angle on slurry erosion. *Wear* **1991**, *141*, 279–289. [CrossRef]
39. Wada, S.; Watanabe, N.; Tani, T. Solid particle erosion of brittle materials (Part 6)—The erosive wear of Al_2O_3-SiC composites. *J. Ceram. Soc. Jpn.* **1988**, *96*, 111–118. [CrossRef]
40. Burstein, G.T.; Sasaki, K. Effect of impact angle on the slurry erosion–corrosion of 304L stainless steel. *Wear* **2000**, *240*, 80–94. [CrossRef]
41. ASTM, Standard Test Method for Conducting Erosion Tests by Solid Particle Impingement Using Gas Jets -ASTM G76-13. 2009. Available online: http://www.sis.se/en/external-categories/astm-standards/astm-g76 (accessed on 4 September 2016).
42. Ruff, A.W.; Ives, L.K. Measurement of solid particle velocity in erosion wear. *Wear* **1975**, *35*, 195–199. [CrossRef]
43. Axinte, D.A.; Srinivasu, D.S.; Kong, M.C.; Butler-Smith, P.W. Abrasive waterjet cutting of polycrystalline diamond: A preliminary investigation. *Int. J. Mach. Tool. Manuf.* **2009**, *49*, 797–803. [CrossRef]
44. Sowards, J.W.; McCowan, C.N.; Drexler, E.S. Interpretation and significance of reverse chevron-shaped markings on fracture surfaces of API X100 pipeline steels. *Mater. Sci. Eng. A* **2012**, *551*, 140–148. [CrossRef]
45. Okonkwo, P.C.; Shakoor, R.A.; Ahmed, E.; Mohamed, A.M.A. Erosive wear performance of API X42 pipeline steel. *Eng. Fail. Anal.* **2016**, *60*, 86–95. [CrossRef]

46. Islam, M.A.; Alama, T.; Farhata, Z.N.; Mohamed, A.; Alfantazi, A. Effect of microstructure on the erosion behavior of carbon steel. *Wear* **2015**, *332–333*, 1080–1089. [CrossRef]
47. Heuer, J.K.; Stubbins, J.F. An XPS characterization of $FeCO_3$ films from CO_2 corrosion. *Corros. Sci.* **1999**, *41*, 1231–1243. [CrossRef]
48. Djebaili, K.; Mekhalif, Z.; Boumaza, A.; Djelloul, A. XPS, FTIR, EDX, and XRD Analysis of Al_2O_3 Scales Grown on PM2000 Alloy. *J. Spectrosc.* **2015**, *2015*. [CrossRef]
49. Zhang, S.; Pang, X.; Wang, Y.; Gao, K. Corrosion behavior of steel with different microstructures under various elastic loading conditions. *Corros. Sci.* **2013**, *75*, 293–299. [CrossRef]
50. Hashish, M. A modeling study of metal cutting with abrasive waterjets. *J. Eng. Mater. Technol.* **1984**, *106*, 88–100. [CrossRef]
51. Finnie, I. Some reflections on the past and future of erosion. *Wear* **1995**, *186–187*, 1–10. [CrossRef]
52. Gomes-Ferreira, C.; Ciampini, D.; Papini, M. The effect of inter-particle collisions in erosive streams on the distribution of energy flux incident to a flat surface. *Tribol. Int.* **2004**, *37*, 791–807. [CrossRef]
53. Shirazi, S.A.; Mclaury, B.S. Erosion modeling of elbows in multiphase flow. In Proceedings of the 2000 ASME Fluids Engineering Summer Meeting, Boston, MA, USA, June 2000; pp. 11–15.